

www.advenergymat.de

Optimizing Ion Pathway in Titanium Carbide MXene for Practical High-Rate Supercapacitor

Jun Tang, Tyler Mathis, Xiongwei Zhong, Xu Xiao, Hao Wang, Mark Anayee, Feng Pan,*
Baomin Xu,* and Yury Gogotsi*

The lengthened ion pathway in restacked 2D materials greatly limits the electrochemical performance of practically dense film electrodes (mass loading >10 mg cm⁻²). Typical strategies such as the insertion of nanomaterials and 3D-structure design is expected to reduce the volumetric capacitance of Ti₃C₂T_x electrodes, diminishing the dominating advantage of Ti₃C₂T_x over other electrode materials. Here, a novel, facile, and controllable H2SO4 oxidation method is developed for alleviating the restacking issue of Ti₃C₂T_x film with few electrochemically inactive side-products such as TiO₂. A hierarchical ion path "highway" in Ti₃C₂T_x film is fabricated with porous structure, atomiclevel increased interlayer spacing, and reduced flake size (through probesonication). As a result, ultra-high rate performance is obtained with high volumetric capacitance. For a ≈1.1 μm thick Ti₃C₂T_x film, capacitance retention of 64% is obtained (208 F g^{-1} /756 F cm⁻³) when the scan rate is increased from 5 to 10,000 mV s⁻¹. Even at higher mass loadings exceeding 12 mg cm⁻² (48 µm thickness), the rate capability is still comparable to unoptimized Ti₃C₂T_x electrodes with low mass loading (1 mg cm⁻²). Consequently, a high areal capacitance of ≈3.2 F cm⁻² is achieved for pathway-optimized thick Ti₃C₂T_x film, which is of great significance for practical applications.

1. Introduction

Transition metal carbide, nitrides, and carbonitrides (MXenes) are a rapidly growing class of 2D materials that have been intensively studied for diverse applications, such as energy storage, electromagnetic interference shielding, transparent conductive electrodes, environmental and water treatment, catalysis, sensors, and biochemical applications. $^{[1-13]}$ $Ti_3C_2T_x$ (T_x refers to -Cl, -F, -OH, and =O) is the first reported and most studied

MXene for supercapacitor application which shows outstanding proton-induced pseudocapacitance in acidic aqueous electrolytes.^[14,15] High electronic conductivity (up to 15 000 S cm⁻¹), high packing density (up to 4 g cm⁻³), along with high pseudocapacitance endow Ti₃C₂T_x ultrahigh volumetric capacitance (≈1500 F cm⁻³), which gives Ti₃C₂T_x incomparable advantages over other electrode materials for supercapacitors.^[16] However, electrodes suffer from long ion transport pathways due to the stacking nature of 2D materials, leading to ultra-low rate performance in a thick electrode. When used as a power supply for electronic devices where high areal energy densities at high rates are required, MXene electrodes need to be thick enough to ensure high charge storage capability. In this context, the ion transport issue becomes more critical because the low rate performance will deteriorate with the increase of film thickness.[17]

Numerous efforts have been made to alleviate the restacking issue of ${\rm Ti}_3{\rm C}_2{\rm T}_x$ film electrodes. Typical strategies include interlayer insertion of graphene, carbon nanotube or other nanomaterials, pillared structure design, template sacrifice method, vertical alignment, and etching holes. [17–27] However, by most of the reported approaches, the rate performances are increased at the expense of volumetric capacitance because of the introduction of inactive materials, excess spacing, or active materials with lower volumetric capacitance. For example, \approx 15% decrease

Dr. J. Tang, Dr. T. Mathis, M. Anayee, Prof. Y. Gogotsi
A. J. Drexel Nanomaterials Institute and Department of Materials
Science and Engineering
Drexel University
Philadelphia, PA 19104, USA
E-mail: gogotsi@drexel.edu
Dr. J. Tang, Dr. X. Zhong, Prof. B. Xu
Department of Materials Science and Engineering
Southern University of Science and Technology
Shenzhen, Guangdong Province 518055, China
E-mail: xubm@sustech.edu.cn

The ORCID identification number(s) for the author(s) of this article can be found under https://doi.org/10.1002/aenm.202003025.

DOI: 10.1002/aenm.202003025

Dr. J. Tang, Prof. F. Pan
School of Advanced Materials
Peking University Shenzhen Graduate School
Peking University
Shenzhen, Guangdong Province 518055, China
E-mail: panfeng@pkusz.edu.cn
Prof. X. Xiao
State Key Laboratory of Electronic Thin Film and Integrated Devices
School of Electronic Science and Engineering
University of Electronic Science and Technology of China
Chengdu, Sichuan Province 610054, China
Dr. H. Wang
School of Chemical and Biomedical Engineering
Nanyang Technological University
Singapore 637459, Singapore

www.advancedsciencenews.com

www.advenergymat.de

16146840, 2021, 4, Downloaded from https://advan

onlinelibrary.wiley.com/doi/10.1002/anm.202003025 by University Town Of Shenzhen. Wiley Online Library on [2411/2025]. See the Terms and Conditions (thps://onlinelibrary.wiley.com/terms-and-conditions) on Wiley Online Library for rules of use; OA articles are governed by the applicable Creative Commons.

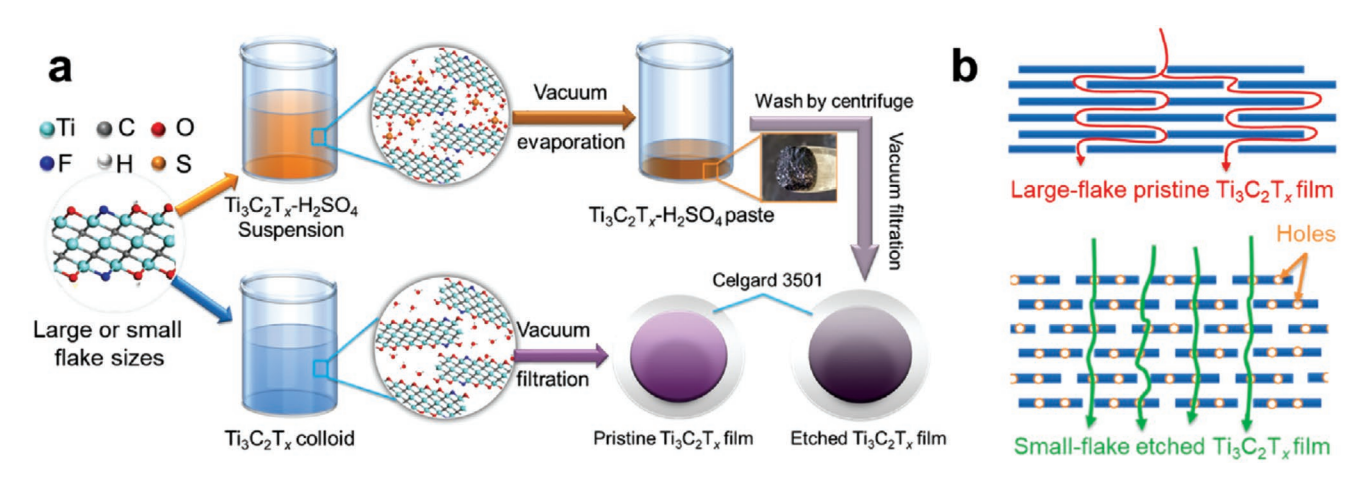


Figure 1. Schematic illustrations of the etching process of $Ti_3C_2T_x$ nanosheets and the obtained hierarchical nanoporous structure. a) Processes for fabricating pristine and etched $Ti_3C_2T_x$ films. The bottom synthesis flow shows a regular $Ti_3C_2T_x$ film fabrication process by vacuum filtration of $Ti_3C_2T_x$ nanosheets from their colloid dispersion. The upper flow shows the etching process in which the $Ti_3C_2T_x$ nanosheets mixed with diluted H_2SO_4 were concentrated by vacuum evaporation in a vacuum oven at \approx 60 °C overnight. The etching process took place in this step. The washed and redispersed $Ti_3C_2T_x$ nanosheets were finally vacuum filtrated into films. b) The schematic illustration of the ion pathway optimization in S-etched $Ti_3C_2T_x$ film comparing with the L-pristine film.

in volumetric capacitance was caused by the incorporation of only 5 wt.% graphene in Ti₃C₂T_x film at a low scan rate of 2 mV s⁻¹.^[21] The introduction of pillaring materials such as ionic liquid or organic molecules will cause more severe gravimetric capacitance fading because the pillared species are almost inactive for charge storage. Both the template sacrifice and vertical alignment methods can greatly improve the rate performance due to the introduction of excess spacings. However, this will result in low packing densities of Ti₃C₂T_x films and accordingly, lead to a decrease in volumetric capacitances. For example, a low packing density of only ≈0.35 g cm⁻³ was obtained by mesoporous Ti₃C₂T_x film synthesized by sacrificing the polymethyl methacrylate (PMMA) microspheres template and the resulted volumetric capacitance is as low as ≈110 F cm⁻³.^[18] By vertical alignment method, the electrolyte ion transport resistance inside Ti₃C₂T_x film has been greatly reduced, which, however, results in a volumetric capacitance lower than 200 F cm⁻³.[23] Holes were generated in MXene to alleviate the restacking issue in our previous work using an in situ anodic oxidation method, by which the introduction of inactive materials can be avoided and improved rate performance was achieved (for $Ti_3C_2T_x$ electrodes with partial oxidation).^[28] However, this in situ electrochemical method is not suitable for large-scale fabrication and the side-products may affect the properties of the electrolyte in a real application where massive electrode material and ultra-low amount of electrolyte are used. Based on the possible universality of oxidation effect on performance improvement, it is considered that the chemical oxidation process may be more effective and applicable for large-scale fabrication of Ti₃C₂T_x with porous structure.

Here, a novel, facile, and scalable chemical approach was reported to construct an "ultimate" structure for ion transport in $\text{Ti}_3\text{C}_2\text{T}_x$ film. For the first time, we showed that $\text{Ti}_3\text{C}_2\text{T}_x$ nanosheets could be partially etched by concentrated H_2SO_4 oxidation without affecting or destroying the crystal structure of the unetched part, which meanwhile resulted in an atomic increase of interlayer spacing. Finally, an "ultimate" structure

was constructed by introducing probe sonication before the concentrated H₂SO₄ etching process, where Ti₃C₂T_x films with increased interlayer spacing were assembled by porous Ti₃C₂T_r nanosheets with small flake size as shown in Figure 1. As a result, the ion transport can be greatly facilitated in this unique hierarchical ion "highway" and ultrahigh rate performance was achieved. Moreover, owing to the atomic level (≈0.1 nm) of the increase in interlayer spacing, the packing density of the $Ti_3C_2T_x$ films were not significantly reduced by this etching approach, and accordingly, high volumetric capacitances were retained at high rates even in ultra-thick films, showing promising potential towards practical application of Ti₃C₂T_r based supercapacitors. This method may be also applicable to other kinds of MXenes and may, thereby, become a universal technique for modifying and optimizing the structure of 2D MXene nanosheets for various applications.

2. Results and Discussions

 ${\rm Ti_3C_2T_x}$ are typically synthesized by selective etching of Al atoms from the ternary layered ${\rm Ti_3AlC_2}$ phases followed by the delamination process. Freestanding films can be fabricated by vacuum-assisted filtration that utilizes the self-woven effect of the 2D nanosheets (bottom row in Figure 1a). This stacking structure greatly limited the transport of electrolyte ions inside the ${\rm Ti_3C_2T_x}$ film especially in the vertical direction where the overall ion transport is hindered or lengthened by at least 1000 times (assuming that the flake size of single-layer ${\rm Ti_3C_2T_x}$ is $\approx 1~\mu{\rm m}$ and the thickness is $\approx 1~{\rm nm}$). Therefore, etching holes on the ${\rm Ti_3C_2T_x}$ sheets seems to be an effective way to solve the ion transport problem by providing shortcuts in restacked film.

A facile strategy for etching holes on the $Ti_3C_2T_x$ nanosheets is shown in Figure 1a (top row) by simply concentrating (by vacuum evaporation at 60 °C) the mixture of $Ti_3C_2T_x$ - H_2SO_4 dispersion. As-synthesized large-size $Ti_3C_2T_x$ and probe-sonicated $Ti_3C_2T_x$ nanosheets with smaller flake sizes were both etched

16146840, 2021, 4, Downloaded from https://adv

onlinelibrary.wiley.com/doi/10.1002/aemm.202003025 by University Town Of Shenzhen, Wiley Online Library on [24/11/2025]. See the Terms and Conditions (https://onlinelibrary.wiley.com/terms-

conditions) on Wiley Online Library for rules of use; OA articles are governed by the applicable Creative Commons

www.advancedsciencenews.com

www.advenergymat.de

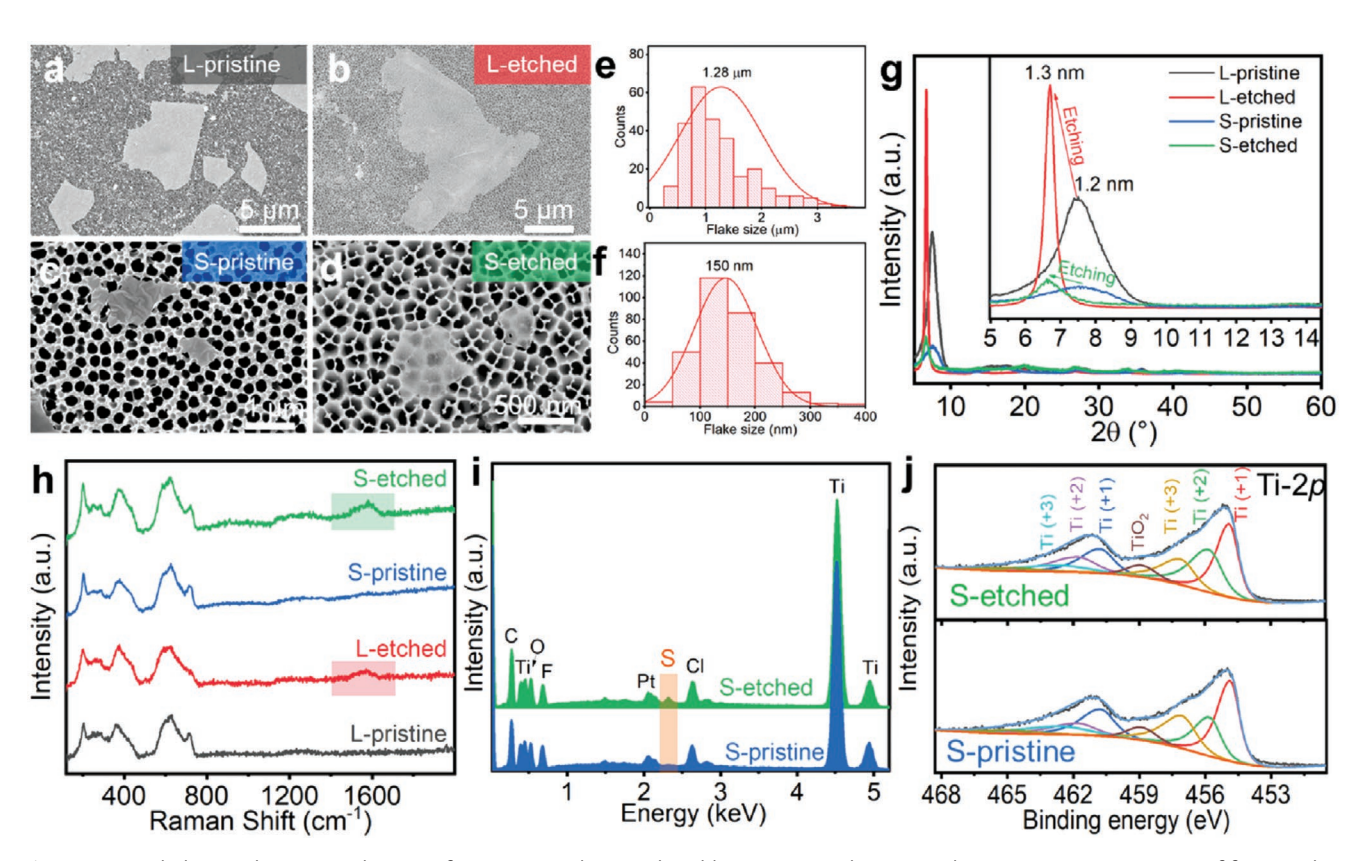


Figure 2. Morphology and structure changes of $Ti_3C_2T_x$ nanosheets induced by concentrated H_2SO_4 etching. SEM top-view images of free-standing films assembled with a) L-pristine, b) L-etched, c) S-pristine, and d) S-etched $Ti_3C_2T_x$ nanosheets. The size distribution of e) L-pristine and f) S-pristine nanosheets. g) XRD patterns and h) Raman spectra of the $Ti_3C_2T_x$ films before and after etching. i) EDS and j) XPS of S-pristine and S-etched $Ti_3C_2T_x$ nanosheets. No titanium oxides were observed after etching from XPS results, indicating successful removal of titanium oxides during the etching or washing process.

for comparison. For convenience, the free-standing films assembled with large pristine, large etched, small pristine, and small etched ${\rm Ti_3C_2T_x}$ nanosheets are named L-pristine, L-etched, S-pristine, and S-etched, respectively. An optimized structure is expected in S-etched ${\rm Ti_3C_2T_x}$ electrodes and the difference between pathways of electrolyte ions in the L-pristine and S-etched films is displayed in Figure 1b. It is hypothetically that the ions transport can be greatly facilitated by the unique hierarchical nanoporous structure in the S-etched film due to the shortened ion pathway and enlarged interlayer spacing. Accordingly, high rate performance can be expected.

It is worth noting that the 2D structure of $Ti_3C_2T_x$ nanosheets is well kept after etching (**Figure 2**a–d), for both large and small size $Ti_3C_2T_x$ nanosheets (with an average flake sizes of 1.28 µm and 150 nm as shown in Figure 2e and f, respectively, which were counted from the scanning electron microscope (SEM) images, Figure S3, Supporting Information). The surface and cross-sectional morphology of the $Ti_3C_2T_x$ films (with similar mass loading) were not significantly changed after etching (Figures S1 and S2, Supporting Information), indicating a possibility of retaining the high packing density (\approx 3.0 mg cm $^{-3}$). Interestingly, after etching in concentrated H_2SO_4 , an atomic level increase in interlayer spacing (\approx 0.1 nm) was observed for both L-etched and S-etched $Ti_3C_2T_x$ films (Figure 2g). The increased interlayer spacing can be ascribed to the residual sulfur compound(s) and carbon species on the surface of etched

Ti₃C₂T_x nanosheets (Figure 2h,i). The sulfur compound(s) (observed by energy dispersive X-Ray spectroscopy (EDS), as shown in Figure 2i) may be physically or chemically adsorbed on the $Ti_3C_2T_x$ surface which were not washed away and the carbon (reflected by Raman results as shown in Figure 2h) may be in situ formed during the etching process where the surface Ti atoms are partially oxidized and etched away. The existing sulfur compound(s) and carbon can then prop up the interlayer spacing when the etched $Ti_3C_2T_x$ nanosheets were assembled into freestanding films and thus, larger interlayer spacing can be obtained by comparing to the pristine ones. Since the increase in interlayer spacing is in the atomic level (one angstrom), high packing density can be retained after etching and thus high volumetric capacitance retains. Moreover, no titanium oxides were observed in the etched Ti₃C₂T_x films (as shown in X-ray photoelectron spectroscopy (XPS), Figure 2j), indicating the removal of titanium oxides during the etching process, which is further verified by the quantitate EDS results (Figure S4, Supporting Information), showing a significant reduction in the Ti/C atomic ratio. Washing away titanium oxides is very important for achieving high capacitance and high rate performance because of their inactivity and limited contribution to the electrochemical performance.

Numerous holes were observed after etching (Figure 3a,c) by comparing the transmission electronic microscope (TEM) images of small $Ti_3C_2T_x$ nanosheets before and after etching.

minelibrary.wiley.com/doi/10.1002/aenm.202003025 by University Town Of Shenzhen, Wiley Online Library on [2411.2025]. See the Terms and Conditions (htps://onlinelibrary.wiley.com/terms-and-conditions) on Wiley Online Library for rules of use; OA articles are governed by the applicable Creative Commons.

Figure 3. Morphology and structure changes of $Ti_3C_2T_x$ nanosheets after etching. TEM images of a,b) S-pristine and c,d) S-etched $Ti_3C_2T_x$ nanosheets. The holes are several nanometers in diameter. The crystal structure of $Ti_3C_2T_x$ around the holes was well retained after etching.

Figure 3b,d shows the high-resolution TEM (HRTEM) images of ${\rm Ti_3C_2T_x}$ nanosheets before and after etching. Both S-pristine and S-etched nanosheets show a lattice fringe spacing of 0.26 nm, corresponding to the (101) interplanar spacing. This result indicates that the crystal structure of unetched ${\rm Ti_3C_2T_x}$ around the holes was not changed during the etching process, which guaranteed the high electron conductivity and high pseudocapacitance of ${\rm Ti_3C_2T_x}$.

A pair of redox peaks were observed in the cyclic voltammetry (CV) profiles of different $Ti_3C_2T_x$ films (**Figure 4**a–d), indicating the pseudocapacitive nature of Ti₃C₂T_x films. Since the crystal structure of unetched Ti₃C₂T_x was not changed, the local electron conductivity can be retained, which ensures fast electron transport at high rates. Therefore, at high rates, the electrochemical performance of Ti₃C₂T_x films will be decided by the ion diffusion and thus the rate performance can be effectively improved by the optimized structure design. To compare the rate performance, the capacitances at different scan rates were calculated from CV results and displayed in Figure 4e. The capacitances of etched Ti₃C₂T_x (both small and large size flake) were slightly increased at a low scan rate of 5 mV s⁻¹, achieving a high capacitance of 324 F g⁻¹, which may be ascribed to the full use of active sites because of the holes generated by etching. At higher scan rates, the etched Ti₃C₂T_x films showed much higher capacitance retentions than the pristine ones. Figure 4e also shows that higher rate performance was achieved by Ti₃C₂T_x films with smaller

flake sizes. Briefly, generating holes (increasing the interlayer spacing at meanwhile) and reducing flake size are both effective ways for improving the rate performance of restacked ${\rm Ti_3C_2T_x}$ films. Specifically, compared to the capacitance at 5 mV s⁻¹, the capacitance retention at 10 000 mV s⁻¹ can be increased to 39.0% from 5.9% by this ion pathway optimization in ${\rm Ti_3C_2T_x}$ films, namely, S-etched films (Figure 4f). The best rate performance was also obtained for S-etched ${\rm Ti_3C_2T_x}$ films with different mass loadings, which shows the validity and repeatability of the structure optimization strategy for improving the electrochemical performance of ${\rm Ti_3C_2T_x}$ (Figure S5, Supporting Information). To compare the charge storage kinetics of pristine and etched ${\rm Ti_3C_2T_x}$ films, the relationship of peak current and the scan rate is displayed in Figure 4g. Given the relationship of

$$i_{p} = a v^{b} \tag{1}$$

where v is the scan rate and i_p is the peak current at different scan rates, a and b are variables.

The kinetics performance can be compared conveniently as the b-value which is reflected in the charge storage kinetics.^[28] The capacitive-type storage gives the value b=1, while the diffusion-limited process gives b=0.5.^[29] Herein, the L-pristine $\mathrm{Ti}_3\mathrm{C}_2\mathrm{T}_x$ film exhibits a highly diffusion-limited process since the b value approaches to b=0.5 line with the increase of scan rate. By etching holes or reducing the flake size, the kinetic properties

16146840, 2021, 4, Downloaded from https

elibrary.wiley.com/doi/10.1002/aenm.202003025 by University Town Of Shenzhen, Wiley Online Library on [24/11/2025]. See the Terms

conditions) on Wiley Online Library for rules of use; OA articles are governed by the applicable Creative Commons

www.advenergymat.de

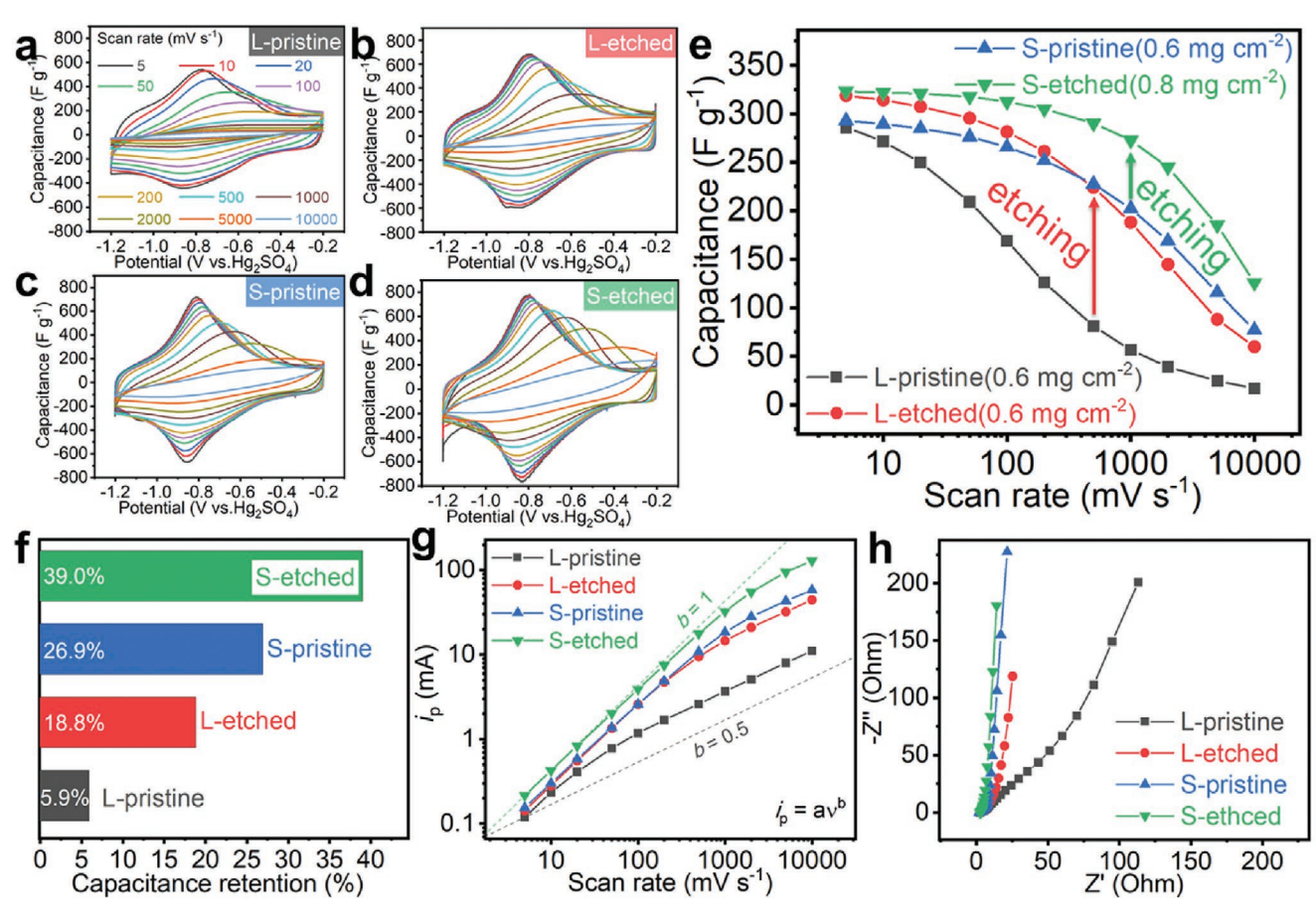


Figure 4. Comparison of electrochemical performance of $Ti_3C_2T_x$ films before and after etching. CV curves of a) L-pristine, b) L-etched, c) S-pristine, and d) S-etched $Ti_3C_2T_x$ films at different scan rates. e) Capacitance versus scan rate, f) capacitance retentions at a high scan rate of 10 000 mV s⁻¹ (compared with the values at 5 mV s⁻¹), g) plots of *b* values, and h) EIS of L-pristine, L-etched, S-pristine, and S-etched $Ti_3C_2T_x$ films.

of $Ti_3C_2T_x$ can be significantly improved since the distance for ion diffusion has been greatly reduced in both ways. By combining both methods, S-etched $Ti_3C_2T_x$ shows a b value close to b=1 line even at high scan rates. The electrochemical impedance spectra (EIS) of pristine and etched $Ti_3C_2T_x$ are shown in Figure 4h, which is highly consistent with the rate performance. By etching holes or reducing flake size, the impedance of $Ti_3C_2T_x$ can be effectively decreased in both low and medium frequency, corresponding to the increased rate performance. The decreased impedance in this frequency range corresponds to the lowering of charge transfer and mass transfer resistances, indicating higher kinetic performance can be obtained for the S-etched $Ti_3C_2T_x$, which contributes to the final rate performance. [28]

To evaluate the rate performance of thick S-etched $\mathrm{Ti_3C_2T_x}$, freestanding films with different areal mass loadings were studied. Figure 5a–g shows the cross-sectional SEM images of the S-etched $\mathrm{Ti_3C_2T_x}$ films with different thicknesses. The relationship between the thickness and mass loading is plotted and displayed in Figure 5h. Obviously, the thickness increases linearly with the increase of mass loading and each film shows a packing density around 3 mg cm⁻³, which is comparable to the packing density of pristine $\mathrm{Ti_3C_2T_x}$ film reported by others. [21,30,31] The high packing density ensured high volumetric capacitance of S-etched $\mathrm{Ti_3C_2T_x}$.

As shown in Figure 6a,b, a high gravimetric/volumetric capacitance of 327 F g⁻¹/≈1200 F cm⁻³ was obtained for the thin S-etched $Ti_3C_2T_x$ film with a thickness of 1.1 μm (mass loading, 0.4 mg cm⁻²). This thin film showed an ultra-high rate performance with a high capacitance of 208 F g⁻¹/756 F cm⁻³ achieved when the scan rate increases to 10 000 mV s⁻¹ (≈64% of the capacitance at a low scan rate of 5 mV s⁻¹). The rate performance decreases with the increase of film thickness. However, even with a high thickness of 48 µm (12 mg cm⁻²), the rate performance of S-etched Ti₃C₂T_x film is still comparable to the L-pristine one with a low mass loading of 1 mg cm⁻² (dash line, Figure 6a). As a result, ultrahigh-energy densities can be obtained at high power densities (Figure S7, Supporting Information). For example, S-etched Ti₃C₂T_x (1.0 mg cm⁻²) shows almost 20 times higher energy density than L-pristine Ti₃C₂T_x at a power density of 100 000 W kg⁻¹. This high mass loading meets the needs of energy storage devices for practical applications and a high volumetric capacitance of 659 F cm⁻³ can be retained in this dense Ti₃C₂T_x film, which can be attributed to the optimized ion pathway structure in the restacked film. Generally, the areal capacitance will increase with the film thickness. However, the increased rate in areal capacitance becomes very slow when the film gets thick enough because it is much difficult for the vertical transport of electrons and ions through www.advancedsciencenews.com

www.advenergymat.de

16146840, 2021, 4, Downloaded from https://advanced.onlinelibrary.wiley.com/doi/10.1002/aemm.202003025 by University Town Of Shenzhen, Wiley Online Library on [24/11/2025]. See the Terms and Conditions (https://onlinelibrary.

onditions) on Wiley Online Library for rules of use; OA articles are governed by the applicable Creative Commons License

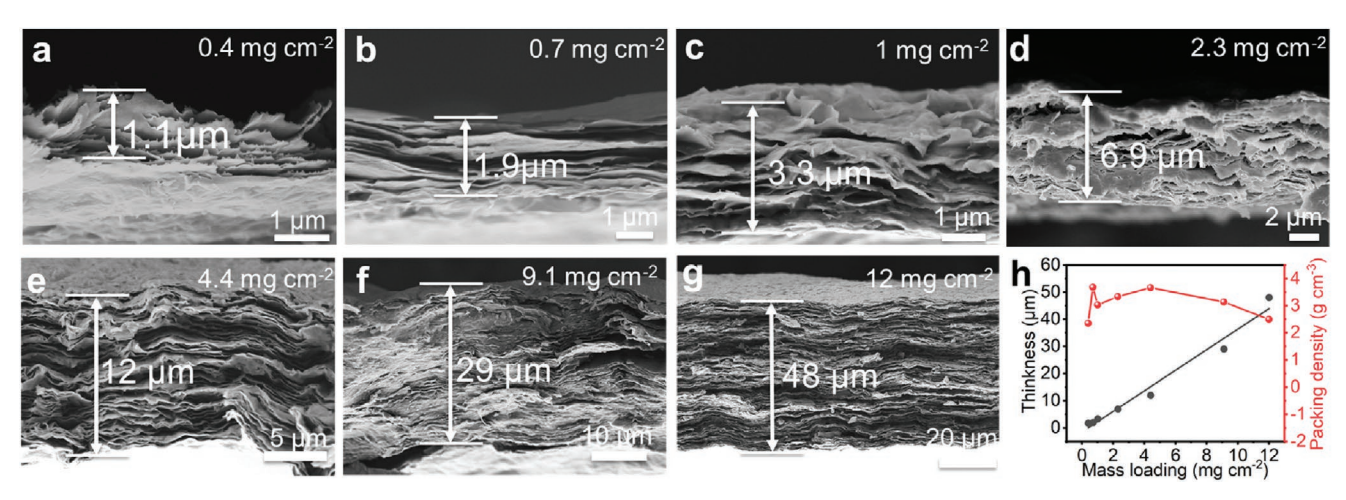


Figure 5. Relationship between areal mass loading and film thickness. Cross-sectional SEM images of S-etched $Ti_3C_2T_x$ films with different areal mass loadings. a) 0.4 mg cm⁻², b) 0.7 mg cm⁻², c) 1.0 mg cm⁻², d) 2.3 mg cm⁻², e) 4.4 mg cm⁻², f) 9.1 mg cm⁻², and g) 12 mg cm⁻². h) A plot showing the relationship of film thickness and packing density with areal mass loading.

the thick film. Here in this work, attributed to the unique hierarchical structure of S-etched ${\rm Ti_3C_2T_x}$ film, the areal capacitance increased significantly with the increase of film thickness, and finally, an ultra-high areal capacitance of 3.2 F cm⁻² was achieved at a film thickness of 48 μ m (12 mg cm⁻²) as shown in Figure 6c, which is of great significance for practical applications. The S-etched ${\rm Ti_3C_2T_x}$ film with a medium thickness of 12 μ m (4.4 mg cm⁻²) was selected for evaluating the cycling stability (Figure 6d). It is shown that 99.3% of the initial capacitance can be retained after 10 000 cycles at a scan rate of 100 mV s⁻¹. By comparing the CV curves before and after

the cycle, a negligible change was observed, indicating an ultrastable cycling performance of S-etched $\mathrm{Ti}_3\mathrm{C}_2\mathrm{T}_x$ film. Accordingly, high rate performance was also retained after the cycle (Figure S11, Supporting Information).

3. Conclusion

For the first time, we report that the $Ti_3C_2T_x$ nanosheets can be partially etched by controlled H_2SO_4 oxidation with few electrochemically inactive side-products. The structure optimized

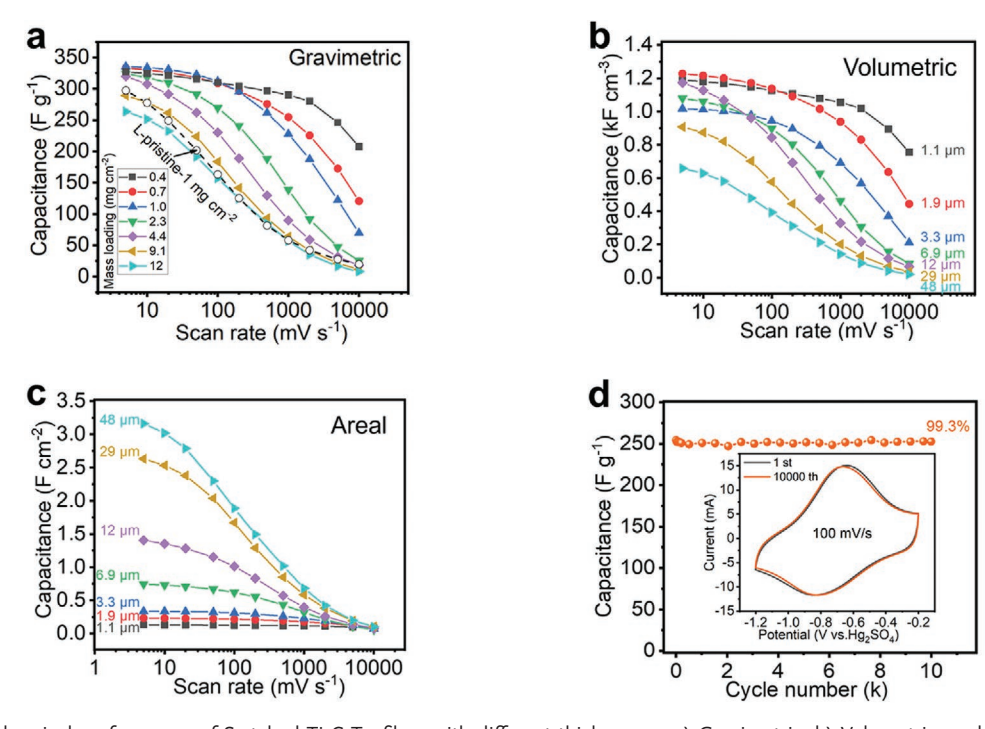


Figure 6. Electrochemical performance of S-etched $Ti_3C_2T_x$ films with different thicknesses. a) Gravimetric, b) Volumetric, and c) Areal rate performance of S-etched $Ti_3C_2T_x$ films. d) Cycling stability of S-etched $Ti_3C_2T_x$ film with a thickness of 12 μ m. Inset: comparison of the CV curve before and after 10 000 cycles.

ADVANCED ENERGY MATERIALS

16146849, 2021, 4, Downloaded from https://advancedonlinelibrary.wiley.com/doi/10.1002/aemm.202003025 by University Town Of Shenzhen, Wiley Online Library on [2411.025]. See the Terms and Conditions (https://onlinelibrary.wiley.com/erms-and-conditions) on Wiley Online Library for rules of use; OA articles are governed by the applicable Creative Commons License

 ${
m Ti}_3{
m C}_2{
m T}_x$ film by concentrated ${
m H}_2{
m SO}_4$ etching combined with probe-sonication achieved ultrahigh electrochemical performance at practical high mass-loadings, demonstrating that reduced flake size, holes on the nanosheets, and increased interlayer spacing (in atomic level) are three key factors for MXenes to alleviate the restacking issue and achieve high electrochemical performances at high rates without sacrificing the volumetric capacitance. It is reasonable to expect that this method can be applied to other MXene family members for structure modification and performance improvement.

4. Experimental Section

Synthesis of Pristine $Ti_3C_2T_x$: $Ti_3C_2T_x$ MXene was synthesized by selective etching of Al atoms from Ti₃AlC₂ (procured from Carbon-Ukraine ltd) using HF/HCl etchant as previously reported.^[28] Briefly, 12 mL of hydrochloric acid (HCl, Fisher Scientific, technical grade, 35-38%), 2 mL hydroflouric acid (Sigma Aldrich, 49%), and 6 mL of deionized (DI) water were mixed by stirring. Then 1 g of Ti₃AlC₂ was slowly added to the solution at 35 °C followed by stirring at 400 rpm for 24 h. The as-obtained suspension (multi-layered MXene) was washed with water via centrifugation at 3500 rpm (5 min per cycle) until pH \geq 6. The sediment was collected and redispersed into 20 mL of water, and then added to the delamination solution containing 1 g LiCl and 40 mL DI water, followed by stirring for 4 h at 400 rpm. The delaminated dispersion was washed using DI water via centrifugation at 7000 rpm until pH ≥ 6. Further, the sediments were redispersed in a small amount of DI water and the high concentration supernatant containing delaminated single- and few-layer Ti₃C₂T_x MXene flakes were collected via centrifugation at 3500 rpm. The concentration of Ti₃C₂T_x dispersion was measured by filtering a specific amount of colloidal solution through a polypropylene filter (3501 Coated PP, Celgard LLC, Charlotte, NC), followed by drying under vacuum at 70 °C overnight and measuring the weight of the solid residue. The high concentration solution was finally diluted into 2.5 mg mL⁻¹ for next-step use. To prepare the $Ti_3C_2T_x$ solution with small flakes size, the high concentration solution was probe sonicated in a cold bath (-10 °C) for 20 min (power: 250 W, and 50% amplitude). The as-obtained solution was then diluted into 2.5 mg mL⁻¹ for next-step use.

Synthesis of Etched $Ti_3C_2T_x$: 2.5 mg mL⁻¹ $Ti_3C_2T_x$ dispersion (with large or small flake size) was mixed with 3m H_2SO_4 with a volume ratio of 1:1 in a bake and then transferred to the vacuum oven and kept at \approx 40 °C for 48 h to remove the water. The as-obtained $Ti_3C_2T_x$ - H_2SO_4 paste was collected and washed via centrifugation at 7000 rpm until pH \geq 6. The solution was finally diluted into 2.5 mg mL⁻¹.

Preparation of Freestanding $Ti_3C_2T_x$ Films: The freestanding pristine or etched MXene films were prepared by vacuum filtration. The films (with a diameter of \approx 4 cm) were dried in a desiccator overnight. The average mass loading of the films was determined by the total amount of $Ti_3C_2T_x$ divided by the area of the film.

Material Characterization: X-ray diffraction (XRD) was performed on a Bruke D8 advance powder X-ray diffractometer equipped with Copper $K\alpha$ radiation ($\lambda=1.540598$ Å). Raman spectra were recorded using a Renishaw Raman microscope with LEICA CTR6000 setup with 633 nm laser, 1200 lines mm^{-1} grating at 10% laser power, and a 50X objective. Spectra were acquired with a dwell time of 90 s with 2 accumulations. The morphology and microstructure of the samples were characterized by an SEM (Zeiss Supra 50VP, Germany) equipped with EDS. TEM images were obtained from FEI Tecnai F30 (300 kV). XPS was conducted using PHI VersaProbe 5000 instrument (Physical Electronics) with a 100 μm and 25 W monochromatic Al-Kα (1486.6 eV) X-ray source. Charge neutralization was accomplished through a dual-beam setup using low energy Ar+ ions and low-energy electrons at 1eV, 200 μA. Samples were sputtered for 3 min at the weakest setting available using 250 V, 1μA for 2 mm × 2 mm area. The data were analyzed with commercially available software, CasaXPS.

Electrochemical Measurements: The Swagelok cell was used for the electrochemical test, with two glass carbon electrodes as current collectors and a Hg/Hg_2SO_4 reference electrode. $Ti_3C_2T_x$ free-standing disc electrodes with a diameter of 3 mm were employed as the working electrodes with over-capacitive activated carbon as the counter electrode. The areal mass loadings of the electrodes were determined by the mass of the electrodes divided by the area of the 3 mm disc. The 3-electrode measurements were performed in 3 m H_2SO_4 electrolytes. The electrochemical tests (CV, galvanostatic charge–discharge (GCD), and EIS) were conducted at room temperature using a VMP3 electrochemical workstation (BioLogic, France). EIS measurements were performed in the frequency range from 100 kHz to 0.1 Hz at open circuit potential by applying a small sinusoidal signal with an amplitude of 10 mV.

Electrochemical Calculations: Gravimetric specific capacitance C_m (F g^{-1}) of electrode materials was calculated from the CV curves by integrating the discharge portion using the following equation:

$$C_{\rm m} = \frac{1}{Vm\nu} \int i \, dV \tag{2}$$

where *i* is the current (mA), *V* is the potential (V), ν is the scan rate (mV s⁻¹), and *m* is the mass of the electrode (mg).

Specific energy density:

$$E_{m} = \frac{1}{m} \int iVdt \tag{3}$$

Specific power density:

$$P_{\rm m} = \frac{E_{\rm m}}{\Lambda t} \tag{4}$$

where m is the mass of the electrode and Δt is the discharge time.

Supporting Information

Supporting Information is available from the Wiley Online Library or from the author.

Acknowledgements

J.T. was sponsored by the China Scholarship Council (CSC). X.X. would like to thank the start-up funding from University of Electronic Science and Technology of China (A1098531023601243). M.A. was supported by the National Science Foundation Graduate Research Fellowship under Grant No. DGE-1646737. Research on electrochemical interfaces at Drexel University was supported by the Fluid Interface Reactions, Structures, and Transport (FIRST) Center, an Energy Frontier Research Center (EFRC) funded by the U.S. Department of Energy, Office of Science, and Office of Basic Energy Sciences. Collaboration between Southern University of Science and Technology (SUSTech) and Drexel University was supported by the Fundamental Research (Discipline Arrangement) Project funding from Shenzhen Science and Technology Innovation Committee (Grant No. JCYJ20170412154554048), the Peacock Team Project funding from Shenzhen Science and Technology Innovation Committee (Grant No. KQTD2015033110182370).

Conflict of Interest

The authors declare no conflict of interest.

Keywords

high rate, MXenes, practical thickness, restacking, supercapacitors

Received: September 23, 2020 Revised: November 12, 2020

Published online: December 13, 2020



ADVANCED ENERGY

16146840, 2021, 4, Downloaded from https://advanced.onlinelibrary.wiley.com/doi/10.1002/aenm.202003025 by University Town Of Shenzhen, Wiley Online Library on [24/11/2025]. See the Terms

for rules of use; OA articles are governed by the applicable Creative Commons

www.advancedsciencenews.com www.advenergymat.de

- B. Anasori, Y. Gogotsi, 2D Metal Carbides and Nitrides (MXenes): Structure, Properties and Applications, Springer International Publishing, Cham 2019.
- [2] G. Gao, A. P. O'Mullane, A. Du, ACS Catal. 2017, 7, 494.
- [3] D. Wang, F. Li, R. Lian, J. Xu, D. Kan, Y. Liu, G. Chen, Y. Gogotsi, Y. Wei, ACS Nano 2019, 13, 11078.
- [4] L. Ding, Y. Wei, Y. Wang, H. Chen, J. Caro, H. Wang, Angew. Chem., Int. Ed. 2017, 56, 1825.
- [5] M. Ghidiu, M. R. Lukatskaya, M.-Q. Zhao, Y. Gogotsi, M. W. Barsoum, *Nature* 2014, 516, 78.
- [6] F. Shahzad, M. Alhabeb, C. B. Hatter, B. Anasori, S. M. Hong, C. M. Koo, Y. Gogotsi, *Science* 2016, 353, 1137.
- [7] C. (John) Zhang, V. Nicolosi, Energy Storage Mater. 2019, 16,
- [8] S. J. Kim, H.-J. Koh, C. E. Ren, O. Kwon, K. Maleski, S.-Y. Cho, B. Anasori, C.-K. Kim, Y.-K. Choi, J. Kim, Y. Gogotsi, H.-T. Jung, ACS Nano 2018, 12, 986.
- [9] Y. Xie, Y. Dall'Agnese, M. Naguib, Y. Gogotsi, M. W. Barsoum, H. L. Zhuang, P. R. C. Kent, ACS Nano 2014, 8, 9606.
- [10] D. Er, J. Li, M. Naguib, Y. Gogotsi, V. B. Shenoy, ACS Appl. Mater. Interfaces 2014, 6, 11173.
- [11] X. Xiao, P. Urbankowski, K. Hantanasirisakul, Y. Yang, S. Sasaki, L. Yang, C. Chen, H. Wang, L. Miao, S. H. Tolbert, S. J. L. Billinge, H. D. Abruña, S. J. May, Y. Gogotsi, Adv. Funct. Mater. 2019, 29, 1809001.
- [12] X. Xiao, H. Wang, P. Urbankowski, Y. Gogotsi, Chem. Soc. Rev. 2018, 47, 8744.
- [13] X. Xiao, H. Wang, W. Bao, P. Urbankowski, L. Yang, Y. Yang, K. Maleski, L. Cui, S. J. L. Billinge, G. Wang, Y. Gogotsi, Adv. Mater. 2019, 31, 1902393.
- [14] M. R. Lukatskaya, O. Mashtalir, C. E. Ren, Y. Dall'Agnese, P. Rozier, P. L. Taberna, M. Naguib, P. Simon, M. W. Barsoum, Y. Gogotsi, Science 2013, 341, 1502.
- [15] M. Naguib, M. Kurtoglu, V. Presser, J. Lu, J. Niu, M. Heon, L. Hultman, Y. Gogotsi, M. W. Barsoum, Adv. Mater. 2011, 23, 4248.

- [16] J. Zhang, N. Kong, S. Uzun, A. Levitt, S. Seyedin, P. A. Lynch, S. Qin, M. Han, W. Yang, J. Liu, X. Wang, Y. Gogotsi, J. M. Razal, Adv. Mater. 2020, 32, 2001093.
- [17] H. Wang, J. Li, X. Kuai, L. Bu, L. Gao, X. Xiao, Y. Gogotsi, Adv. Energy Mater. 2020, 10, 2001411.
- [18] M. R. Lukatskaya, S. Kota, Z. Lin, M.-Q. Zhao, N. Shpigel, M. D. Levi, J. Halim, P.-L. Taberna, M. W. Barsoum, P. Simon, Y. Gogotsi, Nat. Energy 2017, 2, 17105.
- [19] Z. Lin, D. Barbara, P.-L. Taberna, K. L. V. Aken, B. Anasori, Y. Gogotsi, P. Simon, J. Power Sources 2016, 326, 575.
- [20] M.-Q. Zhao, C. E. Ren, Z. Ling, M. R. Lukatskaya, C. Zhang, K. L. V. Aken, M. W. Barsoum, Y. Gogotsi, Adv. Mater. 2015, 27, 339.
- [21] J. Yan, C. E. Ren, K. Maleski, C. B. Hatter, B. Anasori, P. Urbankowski, A. Sarycheva, Y. Gogotsi, Adv. Funct. Mater. 2017, 27, 1701264.
- [22] J. Luo, W. Zhang, H. Yuan, C. Jin, L. Zhang, H. Huang, C. Liang, Y. Xia, J. Zhang, Y. Gan, X. Tao, ACS Nano 2017, 11, 2459.
- [23] Y. Xia, T. S. Mathis, M.-Q. Zhao, B. Anasori, A. Dang, Z. Zhou, H. Cho, Y. Gogotsi, S. Yang, *Nature* 2018, 557, 409.
- [24] P. Simon, ACS Nano 2017, 11, 2393.
- [25] Y. Tang, J. Zhu, C. Yang, F. Wang, J. Electrochem. Soc. 2016, 163, A1975
- [26] J. Tang, W. Yi, X. Zhong, C. (John) Zhang, X. Xiao, F. Pan, B. Xu, Energy Storage Mater. 2020, 32, 418.
- [27] T. Shang, Z. Lin, C. Qi, X. Liu, P. Li, Y. Tao, Z. Wu, D. Li, P. Simon, Q.-H. Yang, Adv. Funct. Mater. 2019, 29, 1903960.
- [28] J. Tang, T. S. Mathis, N. Kurra, A. Sarycheva, X. Xiao, M. N. Hedhili, Q. Jiang, H. N. Alshareef, B. Xu, F. Pan, Y. Gogotsi, Angew. Chem., Int. Ed. 2019, 58, 17849.
- [29] H. Lindström, S. Södergren, A. Solbrand, H. Rensmo, J. Hjelm, A. Hagfeldt, S.-E. Lindquist, J. Phys. Chem. B 1997, 101, 7717.
- [30] M.-Q. Zhao, X. Xie, C. E. Ren, T. Makaryan, B. Anasori, G. Wang, Y. Gogotsi, Adv. Mater. 2017, 29, 1702410.
- [31] T. H. Park, S. Yu, M. Koo, H. Kim, E. H. Kim, J.-E. Park, B. Ok, B. Kim, S. H. Noh, C. Park, E. Kim, C. M. Koo, C. Park, ACS Nano 2019, 13, 6835.